Research Article | Vol. 13, No. 9 / September 2026 / Optica 1903

OPTICA

Direct volumetric reconstruction for highly compressive X-ray fluorescence ghost tomography

A. BEN-YEHUDA,[1] A. RACK,[2] S. SHWARTZ,[1,*] AND N. VIGANÒ[3]

[1]Physics Department and Institute of Nanotechnology and Advanced Materials, Bar Ilan University, Ramat Gan 52900, Israel
[2]ESRF—The European Synchrotron, Grenoble 38043, France
[3]Université Grenoble Alpes, CEA, IRIG-MEM, Grenoble 38000, France
*sharon.shwartz@biu.ac.il

Received 14 April 2026; revised 3 August 2026; accepted 5 August 2026; published 11 September 2026

X-ray fluorescence (XRF) enables element-specific, nondestructive imaging, but conventional raster scanning scales poorly with sample size, particularly for tomography, because measurements must be repeated at every projection angle and spatial position. We demonstrate direct volumetric XRF ghost tomography, which replaces point-by-point acquisition with compressive structured illumination and multiplexed fluorescence detection. Rather than reconstructing projections at each angle and then applying standard tomographic reconstruction, we recover the 3D elemental distribution by solving a single inverse problem that jointly incorporates measurements from all angles. For a volume of 2.8 million voxels, we reconstruct the elemental distribution from only 400 measurements per angle, achieving a 43× reduction relative to raster scanning while maintaining spatial resolution and contrast. By exploiting sparsity directly in the volumetric domain, this approach enables scalable, multi-element XRF tomography of large and heterogeneous samples under stringent acquisition time constraints.

https://doi.org/10.1364/OPTICA.601674

1. INTRODUCTION

X-ray fluorescence (XRF) microscopy is a cornerstone of quantitative chemical mapping, providing element-specific contrast in two and three dimensions across a broad range of length scales, from tens of nanometers to centimeters [1–9]. It plays a central role in sample characterization in fields ranging from materials science [10] and chemistry [11] to cultural heritage studies [12]. The elemental specificity of XRF stems from core-level electronic transitions: following inner-shell excitation, atoms relax by emitting fluorescent photons at characteristic energies determined by the atomic species. Energy-dispersive detectors resolve these fluorescence lines in the recorded XRF spectra, enabling unambiguous elemental identification. In practice, local XRF spectra, typically acquired using a narrow (pencil-beam) raster scan, are analyzed to reconstruct quantitative spatial maps of chemical composition [13]. In such schemes, each beam position corresponds to a pixel in the reconstructed hyperspectral image.

While conceptually straightforward, this sequential acquisition scales poorly with field-of-view (FoV) and resolution. The bottleneck is amplified in tomography, where a complete raster scan of the entire FoV must be repeated at each projection angle. For complex samples with a large number of voxels, this leads to prohibitively long acquisition times, often incompatible with synchrotron beamtime constraints. Moreover, tight focusing produces a high local dose rate, which can introduce radiation damage, heating, sample deformation, and drift that degrades image quality [14].

Computational ghost imaging (CGI) is an imaging technique that reconstructs images computationally from measurements acquired under a sequence of spatially structured illumination patterns [15–19]. Since its introduction, CGI has evolved from correlation-based methods to compressive sensing and model-based reconstruction frameworks, improving reconstruction quality, reducing the number of required measurements, and expanding its applicability across a wide range of imaging modalities, including optical [20], terahertz [21], infrared [22], and X-ray imaging [23]. Previous work has demonstrated that computational imaging approaches, including coded apertures and CGI, can substantially reduce the number of measurements required for XRF imaging [9,24–27]. In XRF-CGI, a single-pixel, energy-resolving detector records the fluorescence spectrum for each illumination pattern, and elemental maps are reconstructed from the measured signals together with the known illumination patterns [9,25]. For objects exhibiting sparse or compressible representations, CGI leverages compressive sensing (CS) [19,28] to substantially reduce the number of measurements required compared with conventional raster-scanning XRF, making large-area elemental imaging and tomography more practical.

For XRF tomography, however, most existing approaches reconstruct each projection independently before performing tomographic reconstruction. Consequently, the reconstruction cannot exploit the strong correlations between projections acquired at neighboring angles, which typically differ only by small spatial changes. This prevents the reconstruction from taking advantage of the volumetric redundancy during the projection reconstruction stage, limiting the achievable measurement compression (Section 8 of Supplement 1). A direct (one-step) 3D reconstruction, introduced in the context of ghost tomography by Kingston *et al.* [29], instead jointly reconstructs the object from measurements acquired at all projection angles by solving a single inverse problem. By enforcing sparsity directly in the reconstructed volume, this formulation exploits the volumetric redundancy of the dataset, enabling substantially higher measurement compression. For XRF tomography, the full potential of direct volumetric reconstruction is realized when combined with CGI, whose multiplexed structured-illumination measurements provide the redundancy required for highly compressive global reconstruction.

Here, we implement this framework for X-ray fluorescence ghost tomography (XRF-GT) and demonstrate its experimental realization within a tailored compressive-sensing scheme. We recover 3D elemental maps of $164 \times 164 \times 105 = 2,824,080$ voxels from only 400 structured-illumination realizations per angle. With 276 angles, this corresponds to 110,400 total measurements, compared with 4,752,720 required for full angular coverage by pencil-beam scans (43× compression). This approach enables practical XRF tomography of large, heterogeneous samples, for which raster-scan and two-step ghost tomography pipelines become prohibitive even at state-of-the-art facilities.

2. EXPERIMENTAL SETUP

The experimental configuration is shown in Fig. 1. A structured mask mounted on a motorized translation stage is positioned upstream of the sample. For each GI realization, the incident beam illuminates a different region of the mask, generating a distinct structured illumination pattern at the sample plane. The sample is mounted on a rotation stage for tomographic acquisition. Downstream of the sample, a 2D imaging detector records the transmitted intensity, while a silicon drift detector (SDD), placed adjacent to the sample and approximately orthogonal to the incident beam direction, records the XRF signal.

We performed the experiment at beamline ID19 of the European Synchrotron Radiation Facility (ESRF) using a broadband incident beam centered at 35 keV with dimensions of 2 mm × 1.2 mm. The sample consisted of Cu wires (40 μm diameter), Zr sheets (20 μm thickness), and spherical Ag particles (maximum particle size 45 μm), embedded in epoxy resin containing light trace elements.

To generate structured illumination, we translated the mask, composed of a monolayer of randomly distributed W (tungsten) powder (particle sizes ranging from 50 to 250 μm), in 0.06 mm steps, producing 900 distinct realizations with an estimated effective feature size of 37 ± 13 μm (Section 11 of Supplement 1). For each mask position, we acquired a full tomographic scan by rotating the sample over 360° in 0.65° increments, yielding 552 projection angles per realization. This angular sampling exceeded that required for the 164×164 reconstruction grid. Therefore, we binned the data by a factor of two along the angular dimension, resulting in 276 projection angles per mask realization. To minimize mismatches caused by beam drift and flux fluctuations, we operated the XRF and imaging detectors simultaneously at every angle. We then integrated the XRF spectra (see Section 2 of Supplement 1) for 0.1 s per angle [25].

3. DATA PROCESSING AND RECONSTRUCTION

The reconstruction workflows of the direct and conventional two-step XRF-GT approaches are illustrated in Fig. 2. In the two-step XRF-GT scheme [Fig. 2(a)], element-specific 2D ghost projections are first reconstructed independently for each rotation angle, followed by a standard tomographic inversion to obtain the 3D elemental distribution. In contrast, the direct XRF-GT [Fig. 2(b)] recovers the 3D elemental volume directly from the raw measurements by solving a single 3D inverse problem.

The two approaches differ in how sparsity is enforced: the two-step pipeline reconstructs projections independently at each angle, whereas the direct formulation imposes sparsity directly in the volumetric domain and jointly incorporates all measurements across masks and projection angles. We formulate the direct reconstruction as the minimization problem:

$$\hat{x} = \underset{x}{\operatorname{argmin}} \left\{ \frac{1}{2} ||MRx - b||_2^2 + \lambda \, ||Hx||_1 \right\}, \qquad (1)$$

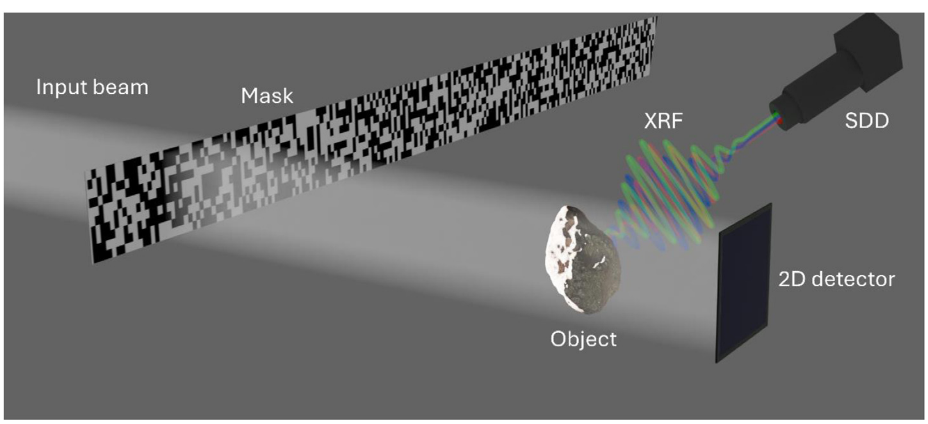

Fig. 1. Schematic of the experimental setup. A tungsten mask modulates the incident beam, generating spatially random illumination patterns that irradiate the object. The transmitted intensity is recorded by a 2D detector, while the emitted fluorescence is collected by an SDD. Both signals are acquired simultaneously as the sample is rotated. Each fluorescence measurement integrates contributions from the entire illuminated region, thereby encoding global spatial information. Element-specific images are reconstructed computationally from correlations between the known illumination patterns and the measured signals, in contrast to raster-scanning XRF, where spatial information is acquired point by point.

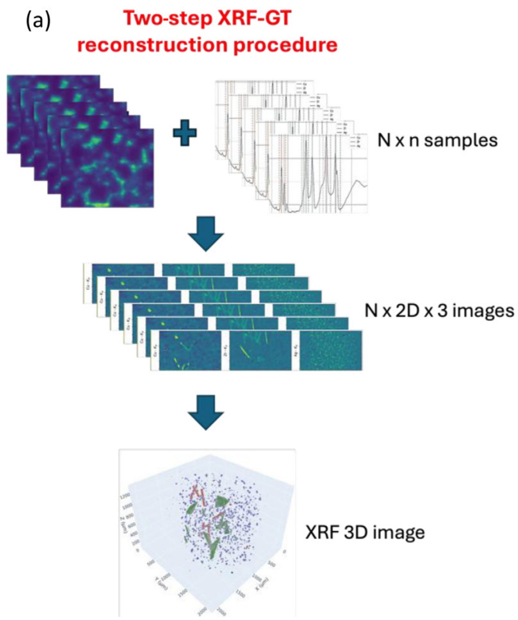

Fig. 2. Comparison between conventional two-step XRF-GT and direct XRF-GT volumetric reconstruction. In the standard approach, angle-resolved ghost projections are first reconstructed independently and subsequently combined via tomographic inversion. In contrast, the direct approach recovers the 3D elemental distribution by solving a single inverse problem that jointly incorporates measurements from all projection angles. This formulation leverages the multiplexed nature of structured illumination in CGI, where each measurement encodes global spatial information. This inherent redundancy enables compressive reconstruction and allows sparsity to be enforced directly in the volumetric domain, in contrast to raster scanning XRF, where measurements are localized and do not provide such redundancy.

where $\hat{x}$ is the reconstructed elemental distribution, R is the Radon transform preceding the CGI projection operator M, b is the vector of measured fluorescence signals, and λ controls the influence of the sparsity prior. The operator H corresponds to the pointwise modulus of the gradient:

$$H(\cdot) := |\nabla(\cdot)| : \mathbb{R}^3 \rightarrow \mathbb{R}, \quad (2)$$

which implements total-variation (TV) regularization. A general sparse-reconstruction formulation is presented in Section 6 of Supplement 1, the corresponding direct XRF-GT formulation is given in Section 7 of Supplement 1, and an illustrative comparison of sparsity in the reconstruction and projection domains is provided in Section 8 of Supplement 1. The regularization weight λ is selected via cross-validation (Section 12 of Supplement 1) to balance sparsity enforcement and preservation of the fine structural details.

4. RESULTS

We demonstrate that direct XRF-GT reconstructs a 3D elemental map of the sample using only 400 structured-illumination measurements per angle. By comparison, an equivalent pencil-beam XRF scan at the same voxel grid would require 17,220 (105×164) beam positions per angle, corresponding to a $43\times$ reduction in measurements. The isosurface rendering in Fig. 3 reveals Cu wires, Zr foils, and Ag particles at their expected locations, with no visible streaking or structured reconstruction artifacts.

To validate our approach, we compare the direct reconstructions with the conventional two-step XRF-GT pipeline and with an independent transmission tomogram (Fig. 4). Figures 4(a)–4(c) show representative tomographic slices reconstructed from 400 realizations per projection angle. At this sampling level, the direct

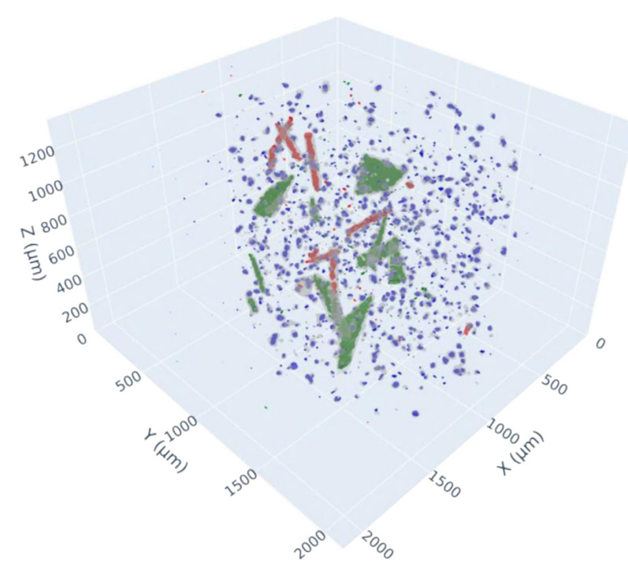

Fig. 3. 3D isosurface rendering of the reconstructed sample. Direct XRF-GT reconstruction of Cu, Zr, and Ag from 400 structured-illumination measurements per angle, shown in red, green, and blue, respectively, overlaid on the transmission tomogram shown in gray.

reconstruction exhibits only about a 10% reduction in image quality relative to the fully sampled case (Section 1 of Supplement 1). More importantly, it still reveals well-defined features that can be readily compared with the corresponding transmission slice. In contrast, the two-step reconstruction shows pronounced background fluctuations, giving rise to circular artifacts [30] (another example is presented in Section 2 of Supplement 1). The severity of these artifacts correlates with the sparsity of each elemental distribution in the gradient domain (Section 8 of Supplement 1).

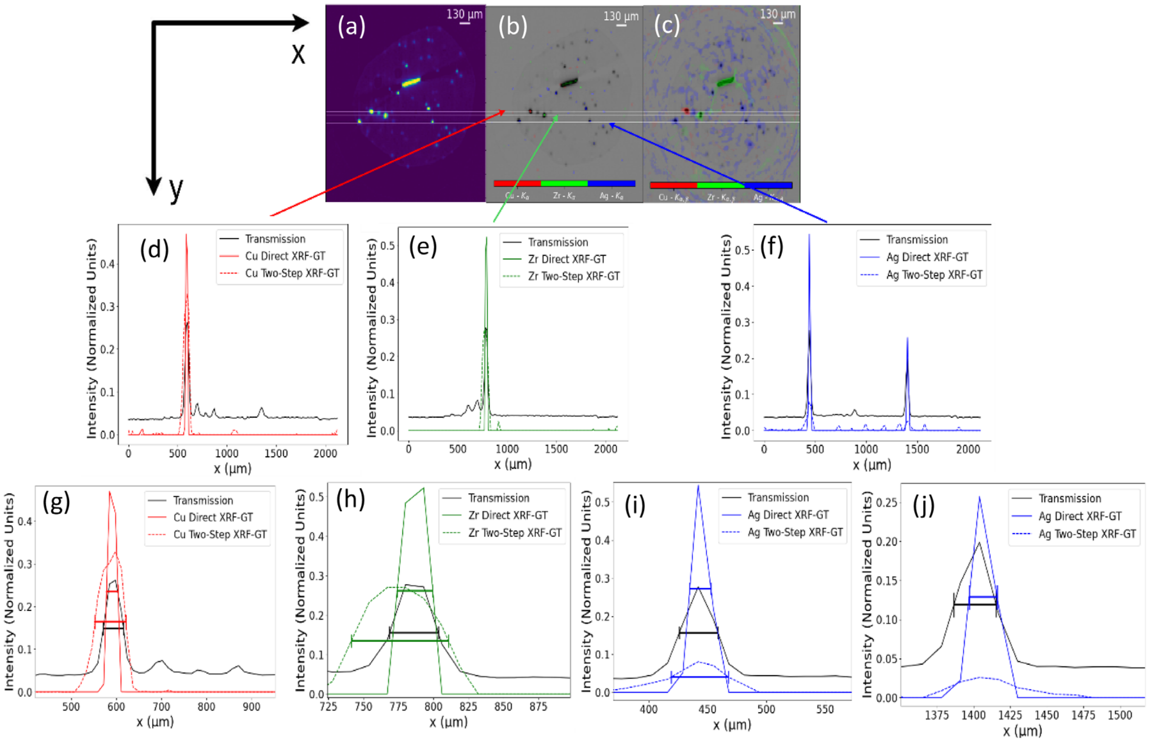

Fig. 4. Tomograms and cross sections. (a) Transmission tomogram, XRF tomograms reconstructed from 400 measurements per angle (b) direct and (c) two-step. (d–f) Corresponding cross sections at $y = 1131, 1170$, and 1248 µm for Cu, Zr, and Ag, respectively, at $z = 975$ µm. Zoomed-in views of the regions indicated by arrows in (a–f): Cu and Zr in (g, h) and Ag in (i, j), where Ag exhibits two peaks. For a fair comparison, the regularization parameter (λ) for the two-step and direct reconstruction methods was selected using an identical hold-out cross-validation procedure (Section 12 of Supplement 1).

Because Ag exhibits the least sparse gradient representation, it is the most susceptible to reconstruction artifacts, whereas Cu, which is the sparsest, is reconstructed with the fewest artifacts. This behavior originates from the fundamental difference between the two reconstruction strategies. In the two-step approach, each tomographic projection is reconstructed independently and therefore cannot exploit the inherent redundancy of the full 3D object. For objects with less sparse gradient representation, this limitation leads to stronger artifacts in the reconstructed projections, which subsequently propagate into the final tomographic volume (Section 8 of Supplement 1). By reconstructing the volume directly rather than through intermediate tomographic projections, the direct approach avoids generating these artifacts in the first place. The distinct morphologies of the Cu wires, Zr foils, and Ag particles enable their identification in the transmission tomogram, and the spatial correspondence with the direct XRF-GT reconstruction confirms the fidelity of the recovered elemental distributions.

We quantify the resolution of our reconstructions using line profiles extracted from identical cross sections, as shown in Figs. 4(d)–4(f). For Cu, Zr, and Ag, the direct reconstruction produces profiles with a full width at half-maximum (FWHM) of 30 ± 13 µm, 30 ± 13 µm, and 20 ± 13 µm, respectively. These values are consistent with the spatial resolution estimated in Section 11 of Supplement 1. The corresponding values obtained with the two-step reconstruction are 70 ± 13 µm, 70 ± 13 µm, and 50 ± 13 µm, respectively, while the transmission tomograms yield 44 ± 13 µm, 35 ± 13 µm, and 33 ± 13 µm, respectively. The cross sections also reveal substantially lower background levels for the direct approach than the two-step pipeline. These differences are most pronounced in low-signal regions, where the two-step approach exhibits elevated background and reduced contrast.

The broader FWHM values obtained with the two-step reconstruction reflect its reduced ability to recover fine structural features compared with the direct approach. By contrast, the FWHM values obtained with direct XRF-GT are comparable, within the experimental uncertainty, to those of the transmission tomogram. The experimental uncertainty is primarily determined by the effective pixel size of the imaging detector.

To further evaluate the quantitative performance of the direct approach under different compression levels, we assessed the relative concentration recovery accuracy [31]. For this dataset, concentration recovery was defined as the percentage of the physical quantity recovered, relative to the fully sampled 900-mask reconstruction:

$$\mathrm{CR} = \left(\frac{\sum_x I_{\mathrm{recon}}(x)}{\sum_x I_{\mathrm{ref}}(x)} \right) \times 100, \tag{3}$$

where CR is the concentration recovery, $I_{\mathrm{recon}}(x)$ is the physical value of the reconstructed volume at voxel x, and $I_{\mathrm{ref}}(x)$ is the physical value of the reference 900-mask reconstruction volume at voxel x.

The results, summarized in Fig. 5, show that while structural boundaries remain well preserved under high compression, the recovered voxel intensity diminishes as the number of mask realizations is reduced. At 400 mask realizations, the relative recovery reaches approximately 65%, 85%, and 78% for Cu, Zr, and Ag, respectively. At stronger compression (100 mask realizations), the recovery falls below 60% for all three elements. These results establish the direct volumetric inversion as an effective strategy

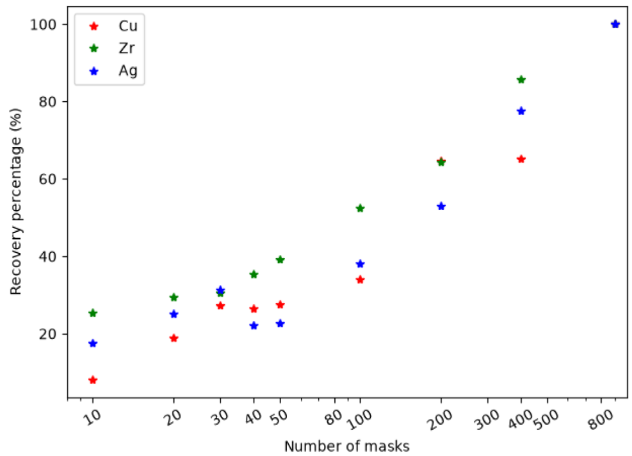

Fig. 5. Relative concentration recovery accuracy as a function of mask count for Cu, Zr, and Ag structures. Recovery is defined as the mean reconstructed intensity normalized to that obtained from the fully sampled 900-mask reconstruction.

for highly compressive XRF tomography while revealing the trade-off between measurement compression and quantitative concentration recovery.

5. DISCUSSION AND CONCLUSION

We have demonstrated XRF-GT using a direct reconstruction framework that jointly inverts measurements across projection angles to recover 3D multi-element distributions. The framework preserves the spatial organization and structural features of the elemental distributions under highly compressive sampling conditions. Using only 400 structured-illumination measurements per angle, we reconstructed elemental distributions comprising 2,824,080 voxels and achieved spatial resolutions of 30 ± 13 μm (Cu), 30 ± 13 μm (Zr), and 20 ± 13 μm (Ag). Compared with pencil-beam scanning-based XRF tomography, this corresponds to an effective $43\times$ per-angle compression. More generally, this work illustrates how multiplexed illumination combined with direct volumetric inversion can substantially reduce the measurement burden of XRF tomography.

A central conceptual advantage of the proposed volumetric approach lies in shifting the sparsity constraint from the projection (sinogram) domain to the 3D elemental distribution itself. Since the three-dimensional elemental distribution is typically far sparser than its individual projections, the reconstruction exploits the intrinsic sparsity of the sample rather than that of intermediate data, enabling accurate reconstruction under highly compressive sampling. This behavior is illustrated in Section 8 of Supplement 1. As a result, accurate multi-element 3D XRF tomography can be achieved from significantly fewer measurements, bringing practical synchrotron implementations within realistic beamtime and dose constraints. Beyond the reconstruction algorithm itself, direct XRF-GT replaces sequential point sampling with multiplexed structured illumination that encodes global information across the field of view, fundamentally changing how information is acquired and enabling highly compressive reconstruction.

While direct XRF-GT offers substantial gains in measurement efficiency, several practical considerations remain. Although the proof-of-concept sample used in this work was deliberately designed to minimize attenuation and self-absorption effects, quantitative imaging of larger or denser specimens will require attenuation correction. Because the proposed direct volumetric reconstruction is based on a flexible linear forward model, established attenuation-aware operators developed for conventional XRF tomography (see, for example, [32]) can be incorporated directly into the forward operator, providing a natural extension of the present framework. Furthermore, samples with more complex or continuously varying elemental distributions, such as biological or geological specimens, may require increased sampling or alternative regularization strategies to achieve comparable reconstruction quality. Finally, the joint 3D inversion increases computational and memory requirements, and the resulting data volumes can make straightforward application of machine-learning approaches [33] challenging at present.

Looking forward, improved physics-based modeling, faster solvers, and adaptive illumination strategies may further extend XRF-GT toward higher resolution, larger volumes, and lower-dose operation, enabling studies of more complex samples within shorter acquisition times and lower dose budgets.

Funding. Israel Science Foundation (2208/24); European Synchrotron Radiation Facility (MI-1505).

Acknowledgment. This work was supported by the Israel Science Foundation (ISF), Grant No. 2208/24. We acknowledge the European Synchrotron Radiation Facility (ESRF) for provision of synchrotron radiation facilities under proposal ID MI-1505.

Disclosures. The authors declare no conflicts of interest.

Data availability. The data that support the findings of this study are available from the corresponding author upon reasonable request.

Supplemental document. See Supplement 1 for supporting content.

REFERENCES

1. N. Gustavsson, A. Paulus, I. Martinsson, *et al.*, "Correlative optical photothermal infrared and X-ray fluorescence for chemical imaging of trace elements and relevant molecular structures directly in neurons," Light Sci. Appl. **10**, 151 (2021).
2. P. Liu, C. J. Ptacek, D. W. Blowes, *et al.*, "Characterization of chromium species and distribution during Cr(VI) removal by biochar using confocal micro-X-ray fluorescence redox mapping and X-ray absorption spectroscopy," Environ. Int. **134**, 105216 (2020).
3. P. M. S. Carvalho, F. Leite, A. L. M. Silva, *et al.*, "Elemental mapping of Portuguese ceramic pieces with a full-field XRF scanner based on a 2D-THCOBRA detector," Eur. Phys. J. Plus **136**, 423 (2021).
4. D. Hampai, A. Liedl, G. Cappuccio, *et al.*, "2D-3D μXRF elemental mapping of archeological samples," Nucl. Instrum. Methods Phys. Res. B **402**, 274–277 (2017).
5. K. Tsuji, T. Matsuno, Y. Takimoto, *et al.*, "New developments of X-ray fluorescence imaging techniques in laboratory," Spectrochim. Acta Part B At. Spectrosc. **113**, 43–53 (2015).
6. A. L. M. Silva, S. Cirino, M. L. Carvalho, *et al.*, "Elemental mapping in a contemporary miniature by full-field X-ray fluorescence imaging with gaseous detector vs. scanning X-ray fluorescence imaging with polycapillary optics," Spectrochim. Acta Part B At. Spectrosc. **129**, 1–7 (2017).
7. F. Förste, L. Bauer, K. Heimler, *et al.*, "Quantification routines for full 3D elemental distributions of homogeneous and layered samples obtained with laboratory confocal micro XRF spectrometers," J. Anal. At. Spectrom. **37**, 1687–1695 (2022).
8. L. Yi, M. Qin, K. Wang, *et al.*, "The three-dimensional elemental distribution based on the surface topography by confocal 3D-XRF analysis," Appl. Phys. A **122**, 856 (2016).
9. Y. Klein, O. Sefi, H. Schwartz, *et al.*, "Chemical element mapping by X-ray computational ghost fluorescence," Optica **9**, 63–70 (2022).
10. J. A. Van Bokhoven, T. L. Lee, M. Drakopoulos, *et al.*, "Determining the aluminium occupancy on the active T-sites in zeolites using X-ray standing waves," Nat. Mater. **7**, 551–555 (2008).

11. F. T. Haase, A. Bergmann, T. E. Jones, *et al.*, "Size effects and active state formation of cobalt oxide nanoparticles during the oxygen evolution reaction," Nat. Energy **7**, 765–773 (2022).
12. R. Ploeger and A. Shugar, "Where science meets art," Science **354**, 826–828 (2016).
13. V. A. Solé, E. Papillon, M. Cotte, *et al.*, "A multiplatform code for the analysis of energy-dispersive X-ray fluorescence spectra," Spectrochim. Acta Part B At. Spectrosc. **62**, 63–68 (2007).
14. M. Karuppasamy, F. K. Nejadasl, M. Vulovic, *et al.*, "Radiation damage in single-particle cryo-electron microscopy: effects of dose and dose rate," J. Synchrotron Radiat. **18**, 398–412 (2011).
15. J. H. Shapiro, "Computational ghost imaging," Phys. Rev. A **78**, 061802 (2008).
16. V. Katkovnik and J. Astola, "Compressive sensing computational ghost imaging," J. Opt. Soc. Am. A **29**, 1556–1567 (2012).
17. Y. Bromberg, O. Katz, and Y. Silberberg, "Ghost imaging with a single detector," Phys. Rev. A **79**, 053840 (2009).
18. W. L. Chan, K. Charan, D. Takhar, *et al.*, "A single-pixel terahertz imaging system based on compressed sensing," Appl. Phys. Lett. **93**, 121105 (2008).
19. A. Ben-Yehuda, O. Sefi, Y. Klein, *et al.*, "High-resolution computed tomography with scattered X-ray radiation and a single pixel detector," Commun. Eng. **3**, 39 (2024).
20. B. Sun, M. P. Edgar, R. Bowman, *et al.*, "3D computational imaging with single-pixel detectors," Science **340**, 844–847 (2013).
21. D. Shrekenhamer, C. M. Watts, W. J. Padilla, *et al.*, "Terahertz single pixel imaging with an optically controlled dynamic spatial light modulator," Opt. Express **21**, 12507–12518 (2013).
22. H. C. Liu and S. Zhang, "Computational ghost imaging of hot objects in long-wave infrared range," Appl. Phys. Lett. **111**, 031110 (2017).
23. Y. Klein, K. Sawhney, S. Shwartz, *et al.*, "X-ray computational ghost imaging with single-pixel detector," Opt. Express **27**, 3284–3293 (2019).
24. P. Meyer and T. Salditt, "Full-field X-ray fluorescence imaging based on coded aperture ghost imaging," Opt. Express **33**, 41802–41814 (2025).
25. M. Manni, A. Ben-Yehuda, Y. Klein, *et al.*, "Synchrotron-based x ray fluorescence ghost imaging," Opt. Lett. **48**, 6271–6274 (2023).
26. J. Li, S. Chen, D. Ratner, *et al.*, "Nanoscale chemical imaging with structured X-ray illumination," Proc. Natl. Acad. Sci. **120**, e2314542120 (2023).
27. E. Levinson, R. H. Shukrun, N. Vigano, *et al.*, "Human-organ-scale X-ray fluorescence ghost imaging for radioisotope-free diagnostics," Sci. Rep. (2026).
28. O. Katz, Y. Bromberg, and Y. Silberberg, "Compressive ghost imaging," Appl. Phys. Lett. **95**, 131110 (2009).
29. A. M. Kingston, G. R. Myers, D. Pelliccia, *et al.*, "X-ray ghost-tomography: artefacts, dose distribution, and mask considerations," IEEE Trans. Comput. Imaging **5**, 136–149 (2019).
30. K. A. Mohan, S. V. Venkatakrishnan, L. F. Drummy, *et al.*, "Model-based iterative reconstruction for synchrotron X-ray tomography," in *IEEE International Conference on Acoustics, Speech and Signal Processing (ICASSP)* (IEEE, 2014), pp. 6909–6913.
31. E. Pfaehler, J. R. De Jong, R. A. J. O. Dierckx, *et al.*, "SMART (SiMulAtion and ReconsTruction) PET: an efficient PET simulation-reconstruction tool," EJNMMI Phys. **5**, 16 (2018).
32. N. Roberto Viganò and V. Armando Solé, "Physically corrected forward operators for induced emission tomography: a simulation study," Meas. Sci. Technol. **29**, 034005 (2018).
33. M. Manni, M. Manni, D. Karpov, *et al.*, "Noise2Ghost: self-supervised deep convolutional reconstruction for ghost imaging," Opt. Express **34**, 24787–24804 (2026).